



**HAL**  
open science

# Probing grain size effect in the superelastic Ti-20Zr-3Mo-3Sn alloy using spherical nanoindentation

Y. Zhou, A. Fillon, D. Laillé, T. Gloriant

► **To cite this version:**

Y. Zhou, A. Fillon, D. Laillé, T. Gloriant. Probing grain size effect in the superelastic Ti-20Zr-3Mo-3Sn alloy using spherical nanoindentation. *Materials Characterization*, 2022, 184, pp.111691. 10.1016/j.matchar.2021.111691 . hal-03515139

**HAL Id: hal-03515139**

**<https://hal.science/hal-03515139v1>**

Submitted on 8 Jan 2024

**HAL** is a multi-disciplinary open access archive for the deposit and dissemination of scientific research documents, whether they are published or not. The documents may come from teaching and research institutions in France or abroad, or from public or private research centers.

L'archive ouverte pluridisciplinaire **HAL**, est destinée au dépôt et à la diffusion de documents scientifiques de niveau recherche, publiés ou non, émanant des établissements d'enseignement et de recherche français ou étrangers, des laboratoires publics ou privés.



Distributed under a Creative Commons Attribution - NonCommercial 4.0 International License

## **Probing grain size effect in the superelastic Ti-20Zr-3Mo-3Sn alloy using spherical nanoindentation**

**Y. Zhou, A. Fillon<sup>\*</sup>, D. Lailé, T. Gloriant**

Univ Rennes, INSA Rennes, CNRS, ISCR-UMR 6226, F-35000, Rennes, France

<sup>\*</sup> Corresponding author: Amélie Fillon

Postal address: Univ Rennes, INSA Rennes, CNRS, ISCR-UMR 6226, 20 avenue des Buttes de Coësmes, CS 70839, Rennes Cedex 7, France.

E-mail address: [amelie.fillon@insa-rennes.fr](mailto:amelie.fillon@insa-rennes.fr) (A. Fillon).

## 1 **Abstract**

2 Grain size effect on superelasticity was investigated in Ti-20Zr-3Mo-3Sn alloys for the same  
3 crystallographic texture and for a broad grain size range from 7  $\mu\text{m}$  to 180  $\mu\text{m}$ . The  
4 dependence of superelasticity on grain size was studied by spherical nanoindentation.  
5 Results displayed the same tendency as that observed during tensile tests. The small-sized  $\beta$   
6 grains favored the martensitic transformation, and exhibited the greater superelasticity. It is  
7 confirmed that spherical nanoindentation is capable of characterizing superelasticity and is  
8 sensitive enough to probe grain size effect in superelastic alloys. It is also shown that  $\beta$  grain  
9 size evidently affects indentation hardness and modulus.

10

11 **Keywords:** Titanium alloys; Nanoindentation; Grain size; Superelasticity; Stress-induced  
12 martensitic transformation.

13

## 14 **1. Introduction**

15 Metastable  $\beta$ -Ti alloys are well-known to display superelastic behavior which arises  
16 from a reversible stress-induced martensitic (SIM) transformation between the  
17 body-centered cubic (bcc)  $\beta$  phase and the orthorhombic  $\alpha''$  phase when they are deformed  
18 cyclically upon loading and unloading within the first yielding region of their macroscopic  
19 engineering tensile stress-strain curves [1, 2].

20 The occurrence of SIM transformation in superelastic metastable  $\beta$ -Ti alloys depends  
21 on: (i) the metastability of  $\beta$  phase determined by the concentration of alloying elements; (ii)  
22 the difference between test temperature and martensite start ( $M_s$ ) temperature which  
23 determines the required driving force for the transformation; (iii) the microstructure  
24 characteristics of  $\beta$  phase such as crystallographic texture and grain size. The above variables  
25 are influenced mutually and reciprocally, and can be tailored by the nature and concentration  
26 of alloying elements and by the thermo-mechanical treatment conditions. For instance,  
27 addition of alloying elements strongly affects the  $M_s$  temperature and the transformation  
28 strain which arises from the lattice distortion between the parent  $\beta$  phase and the  
29 stress-induced  $\alpha''$  phase, and subsequently affects the superelastic response. It was reported  
30 that alloying with Zr and Mo elements is effective to increase the superelastic recovery strain  
31 [3, 4]. The texture control is another efficient way to improve the superelasticity since the  
32 martensitic transformation strain is strongly anisotropic and addition of a small amount of Sn,  
33 as low as 1 to 4 at. %, in metastable  $\beta$ -Ti alloys is favorable for developing  $\langle 110 \rangle_\beta$

34 recrystallization texture which is desirable for large transformation strain and subsequently  
35 for large superelastic recovery strain [5]. Addition of Sn is also very effective at suppressing  
36 the formation of athermal  $\omega$  precipitates which adversely affect the superelasticity [6].  
37 Ti-20Zr-3Mo-3Sn (at. %, Ti2033 for short) alloy has been proposed to show excellent  
38 superelasticity, and occurrence of the reversible SIM transformation has been evidenced in  
39 this alloy system by synchrotron X-ray diffraction [7, 8].

40 The superelastic performances of metastable  $\beta$ -Ti alloys are also largely dependent on  
41 the grain size [11-13]. In the last twenty years, research topics on grain refinement in  
42 superelastic alloys have attracted much attention since combinational properties such as  
43 good superelasticity, small hysteresis (low dissipation energy), high cyclic stability and high  
44 fatigue resistance can be expected to achieve so that new potential applications can be  
45 explored [14]. An earlier study conducted by Grosdidier et al. [15] showed that reduced  
46 grain size of the parent  $\beta$  phase lowers the  $M_s$  temperature, and thus increases the critical  
47 stress for triggering the SIM transformation. The free energy change during such  
48 transformation is responsible for the dependence of the triggering stress on grain size [16].  
49 Bian et al. [17] proposed that smaller grain size causes higher grain boundary constraint  
50 which restrains the shear deformation within grain interiors, and thus enhances the plasticity  
51 resistance. It has also been reported that the reduced grain size could lower the martensitic  
52 transformation strain, change the phase transformation path and improve the mechanical  
53 properties of superelastic alloys [11, 18].

54 Bulk mechanical properties of materials are commonly measured under uniaxial  
55 loading conditions such as uniaxial tension or compression. Recently, nanoindentation is  
56 considered as a suitable and powerful technique for the characterization of local mechanical  
57 properties and nanoscale deformation behavior owing to its capability of sensitively probing  
58 indentation responses from small volumes of materials. By coupling with electron  
59 backscattered diffraction (EBSD) analysis, nanoindentation also can be used to evaluate the  
60 superelasticity of targeted individual grains with orientation indexed by EBSD [19]. It offers  
61 an opportunity to independently investigate the influence of grain size on the superelasticity  
62 by dissociating the texture factor.

63 The present study establishes a correlation concerning the capability of characterizing  
64 the superelasticity between tensile testing and nanoindentation measurement, and elucidate  
65 the influence of grain size on the superelasticity, indentation hardness and modulus at local  
66 scale in the metastable  $\beta$  Ti2033 alloy. It would be valuable to use the coherency of  
67 superelastic characteristics measured by macroscopic tensile testing and nanoindentation  
68 technique to facilitate the evaluation of superelasticity on small-sized materials in the

69 absence of the ability to perform macroscopic tensile, compression or bending tests.

## 70 **2. Materials and methods**

71 The Ti2033 alloy ingots were elaborated by cold crucible levitation melting (CCLM)  
72 technique from pure metals, homogenized at 1223 K for 20 h followed by water quenching,  
73 cold-rolled into 0.5 mm thickness sheet with a thickness reduction rate of 95%, and then  
74 machined into flat tensile specimens in dog-bone shape with 3 mm × 15 mm × 0.5 mm  
75 gauge dimensions. These specimens were recrystallized at 973 K, 1073 K and 1173 K for 0.5  
76 h, respectively, followed by water quenching to retain the metastable  $\beta$  phase. The specimens  
77 were denoted as Ti2033-973K, Ti2033-1073K and Ti2033-1173K. It is worth to mention that  
78 the  $\beta$  transus temperature of Ti2033 alloy has been detected by resistivity measurements to  
79 be 963 K [7]. After thermal treatments, the specimens were treated in an HF/ HNO<sub>3</sub> solution  
80 (1/1 ratio) to remove the surface oxide layer.

81 Macroscale mechanical properties of Ti2033 specimens were evaluated by tensile  
82 testing on an INSTRON 3369 tensile machine in a strain control mode at a rate of  $10^{-4}$  s<sup>-1</sup>.  
83 Cyclic tensile tests were conducted at room temperature with a strain increment of 0.5% by  
84 steps until an elongation of 5.0% and each step was followed by a complete stress release.  
85 The tensile direction was chosen parallel to the cold rolling direction. The grain size and  
86 crystallographic orientations of individual grains were identified by EBSD on a scanning  
87 electron microscope (SEM, JEOL JSM 7100F) equipped with an Oxford HKL EBSD system  
88 and were analyzed by the HKL Channel 5 package. The surface of the specimens was  
89 prepared by electrochemical polishing in an electrolyte composed of perchloric acid (6  
90 vol. %) and methanol (94 vol. %) at -15 °C and 0.2 A current for 45 s. Superelastic response  
91 of the Ti2033 alloy in all heat-treated states was investigated by nanoindentation using the  
92 instrumented NHT Anton Paar nanoindentation test system. Nanoindentation measurements  
93 were performed on selected grains along the surface normal direction at different penetration  
94 depths. Spherical indenter with nominal tip radius of 50  $\mu$ m was used and calibrated on fused  
95 silica sample to take into account the real shape of the tip. Individual grains with targeted  
96 orientations were located by an optical microscope attached in the instrumented  
97 nanoindentation test system, with the aid of EBSD orientation maps.

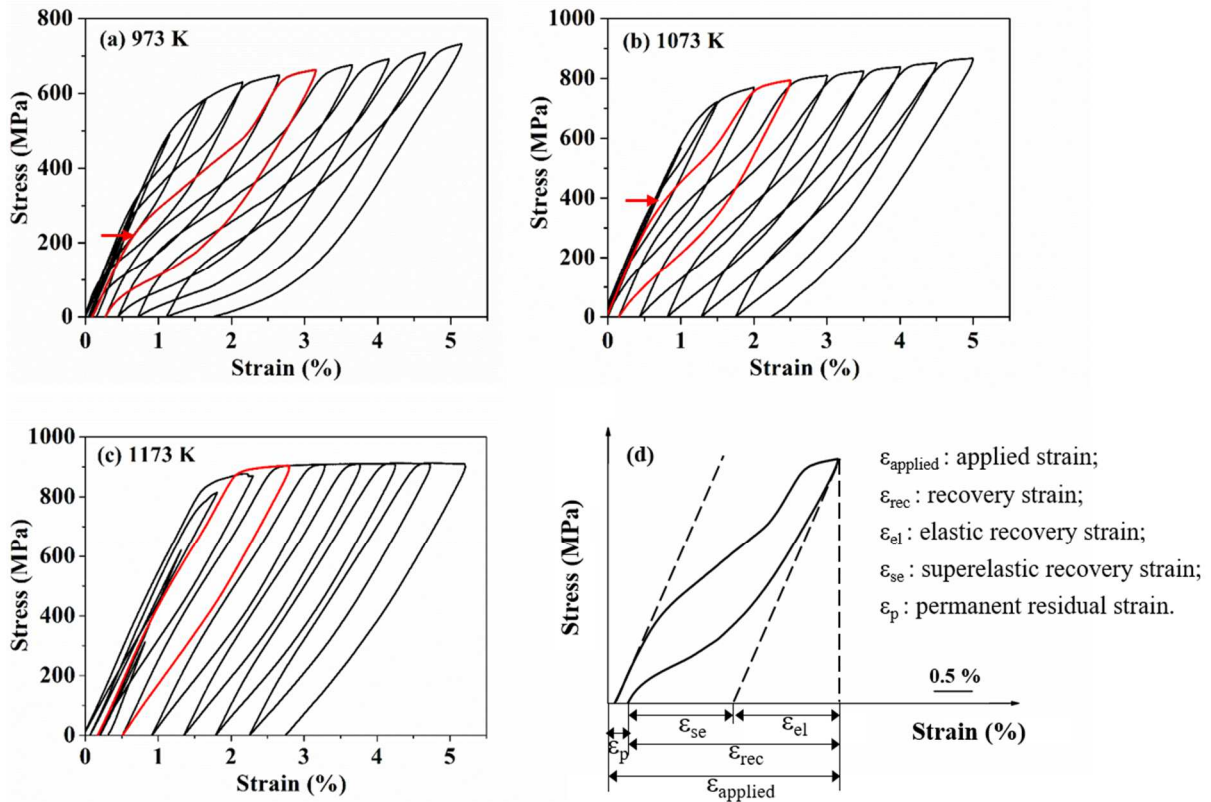
## 98 **3. Results and discussion**

### 99 **3.1 Grain size effect on superelasticity by tensile testing**

100 The tensile cyclic stress-strain curves of Ti2033 specimens recrystallized at 973 K,

101 1073 K and 1173 K for 0.5 h, respectively, are shown in Fig. 1. The stress-strain curves  
 102 exhibit deformation characteristics of the double yielding and the stress hysteresis  
 103 phenomenon associated with the occurrence of reversible SIM transformation between  $\beta$  and  
 104  $\alpha''$  phases [20, 21], demonstrating the superelasticity in Ti2033 alloy. The stress  
 105 corresponding to the first yielding denotes the critical stress for SIM transformation,  $\sigma_{SIM}$ , as  
 106 indicated by the arrow on the cycles highlighted in red. It is noticed that the  $\sigma_{SIM}$  increases  
 107 with increasing heat treatment temperature. The yielding for SIM transformation becomes  
 108 less distinct and the  $\sigma_{SIM}$  cannot be well defined for Ti2033-1173K specimen. The occurrence  
 109 of SIM transformation can be understood regarding the competition among different possible  
 110 accommodating deformation mechanisms in metastable  $\beta$  phase, such as slip, twinning and  
 111 SIM transformation. Thus, SIM transformation is the earlier and dominant mechanism at  
 112 lower grain sizes, and at higher grain sizes the  $\sigma_{SIM}$  tends towards the critical stress for  
 113 dislocation slips  $\sigma_{CSS}$ , masking the SIM transformation altogether.

114 As indicated in Fig. 1d, for each individual loading-unloading cycle, the maximum  
 115 applied strain ( $\epsilon_{applied}$ ), and other four types of strain, elastic recovery strain ( $\epsilon_{el}$ ), superelastic  
 116 strain ( $\epsilon_{se}$ ), total recovery strain ( $\epsilon_{rec}$ ) which is the summation of  $\epsilon_{el}$  and  $\epsilon_{se}$ , and permanent  
 117 residual strain ( $\epsilon_p$ ) after complete unloading were evaluated from the stress-strain curves to  
 118 characterize superelastic properties [5, 9].



119

120 Fig. 1 Tensile cyclic stress-strain curves of Ti2033 specimens recrystallized at (a) 973 K, (b) 1073 K and  
 121 (c) 1173 K for 0.5 h, respectively. The curves were reorganized from [7]. (d) measurement scheme of the

122

different strains from the red cycle presented in (a).

123

124

125

126

127

128

129

130

131

132

133

The magnitudes of total recovery strain  $\varepsilon_{rec}$  and superelastic recovery strain  $\varepsilon_{se}$  extracted from the cyclic stress-strain curves for the three specimens were plotted as a function of applied strain  $\varepsilon_{applied}$  of each cycle (Fig. 2a). The diagonal line in Fig. 2a represents the 100% full recovery. Almost perfect recovery is exhibited up to 2.5% for the Ti2033-973K alloy. At high  $\varepsilon_{applied}$ , the deviation of  $\varepsilon_{rec}$  from the diagonal line indicates the permanently residual strain  $\varepsilon_p$ , due to the occurrence of irreversible martensitic transformation and plastic deformation. For the Ti2033-973K alloy, the total recovery strain  $\varepsilon_{rec}$  firstly increases with increasing  $\varepsilon_{applied}$  until reaches the maximum  $\varepsilon_{rec}$  of 3.5% and also obtains the maximum superelastic recovery strain  $\varepsilon_{se}$  of 2.3%.  $\varepsilon_{rec}$  and  $\varepsilon_{se}$  are clearly higher than those measured for Ti2033-1073K and Ti2033-1173K alloys. The strain recovery ratios were calculated as the ratio of strain recovery to the applied strain on each cycle:

134

$$\eta_{\varepsilon_{rec}} = 100 * \frac{\varepsilon_{rec}}{\varepsilon_{applied}} \quad (1)$$

135

136

137

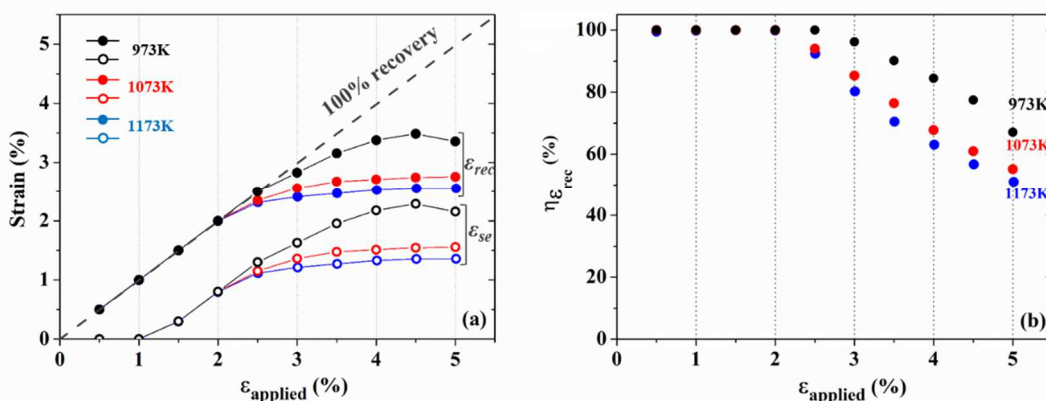
138

139

140

141

The variation of strain recovery ratio  $\eta_{\varepsilon_{rec}}$  with respect to the applied stress  $\varepsilon_{applied}$  at each cycle is presented in Fig. 2b. It shows that the three alloys follow the same tendency: the magnitudes of  $\eta_{\varepsilon_{rec}}$  remain at 100% to a certain strain level and then decrease with the increasing  $\varepsilon_{applied}$ . It also shows that the strain recoverability is dependent on the thermal treatments. It can be concluded that by tensile testing, the recovery performances of the studied specimens behave as the following sequence: Ti2033-973K > Ti2033-1073K > Ti2033-1173K.



142

143

144

145

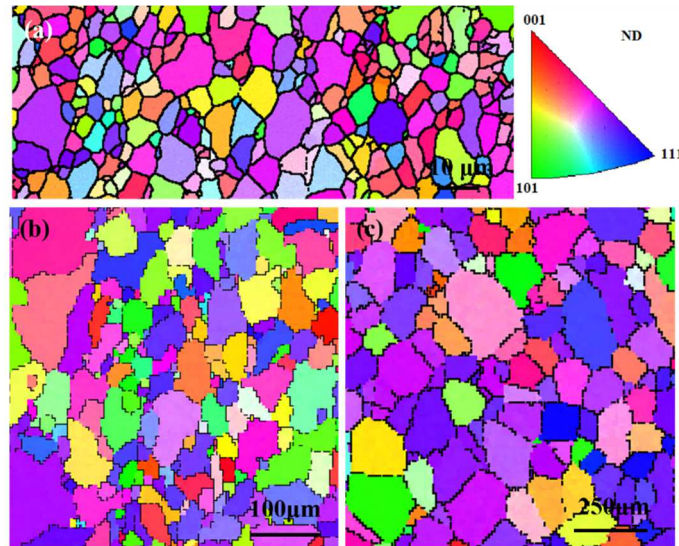
Fig. 2 (a) Total recovery strain  $\varepsilon_{rec}$ , superelastic strain  $\varepsilon_{se}$ , and (b) recovery strain ratios  $\eta_{\varepsilon_{rec}}$  extracted from cyclic loading-unloading tensile curves as shown in Fig.1, and plotted as a function of the applied strain  $\varepsilon_{applied}$  of each cycle.

146

147

The different levels of recoverability in superelastic alloys can be attributed as many influencing factors, such as texture [5, 7, 8, 22, 23], phase composition [5, 24],

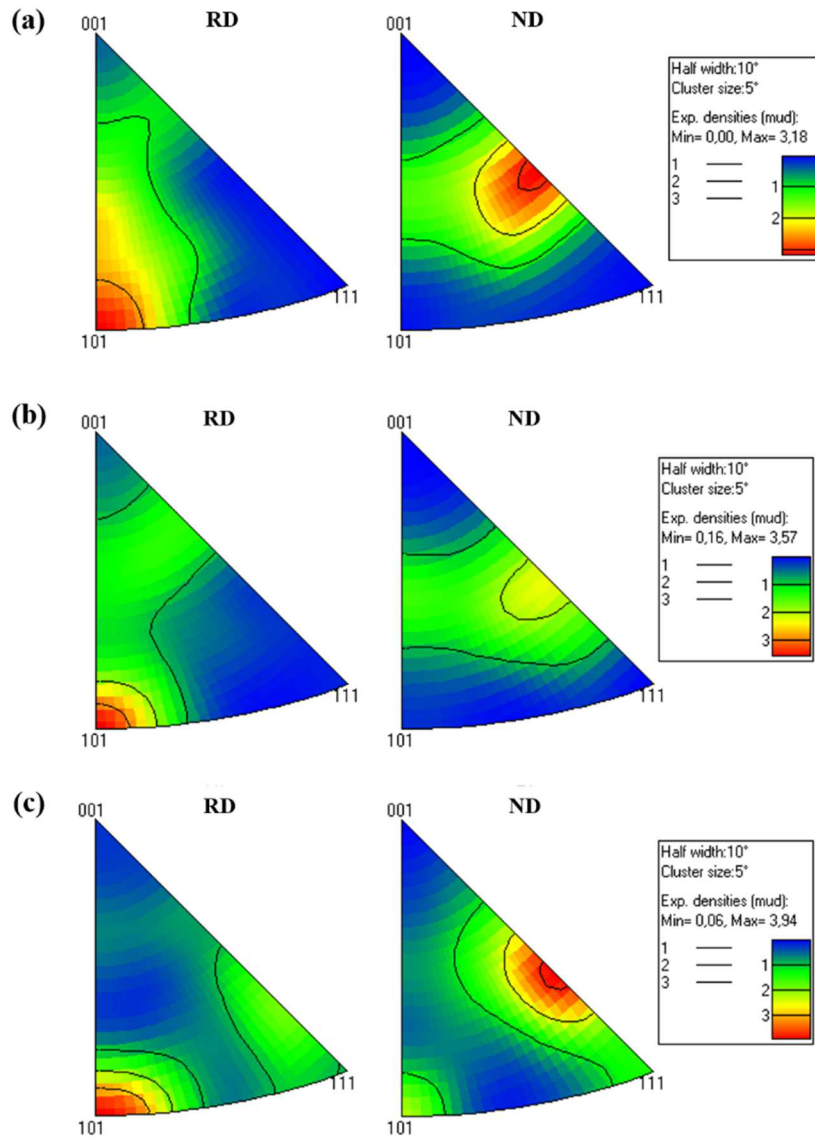
148 transformation strain [23, 25], competition between the critical stresses for SIM  
149 transformation  $\sigma_{SIM}$  and for dislocation slip  $\sigma_{css}$  [13, 24, 26], and grain size [12, 13]. It is  
150 likely that the observed differences in the strain recoverability of Ti2033 alloys arise from  
151 the different heat treatments causing the difference in grain sizes. Thus, it is of great interest  
152 to elucidate the influence of heat treatment temperature on the microstructure and  
153 superelasticity of Ti2033 alloys. Fig. 3 presents the EBSD orientation maps along the normal  
154 direction (ND) for Ti2033 alloys recrystallized at 973K, 1073K, and 1173K. All specimens  
155 display typical equiaxed  $\beta$ -grain microstructures. The average grain size determined from the  
156 EBSD maps was calculated to be 7  $\mu\text{m}$ , 70  $\mu\text{m}$  and 180  $\mu\text{m}$ , for the Ti2033-973K,  
157 Ti2033-1073K, and Ti2033-1173K, respectively, with standard deviation of 2  $\mu\text{m}$ , 16  $\mu\text{m}$  and  
158 41  $\mu\text{m}$ , respectively. That is, grain size decreases with decreasing heat treatment temperature.



159  
160 Fig. 3 EBSD orientation maps along the normal direction (ND) for recrystallized Ti2033 alloys at: (a) 973  
161 K; (b) 1073 K; (c) 1173 K.

162 To furthermore compare the crystallographic orientation of the three specimens, the  
163 corresponding inverse pole figures (IPF) are shown in the rolling direction (RD) and ND for  
164 each specimen in Fig. 4. It can be seen that although the specimens were subjected to  
165 different heat treatments, all displayed the same  $\{113\}_\beta \langle 110 \rangle_\beta$  strong recrystallization  
166 texture. It offers an opportunity to independently investigate the influence of grain size on  
167 the superelasticity by dissociating the texture factor. Therefore, it is reasonable to accept that  
168 during tensile test the increased superelasticity observed in the Ti2033 alloy recrystallized at  
169 lower temperature is predominantly attributed to the reduced grain size. It might be very  
170 interesting to investigate the grain size effect on superelastic behaviors of Ti2033 alloys  
171 under compression at the local scale using nanoindentation.





172  
173

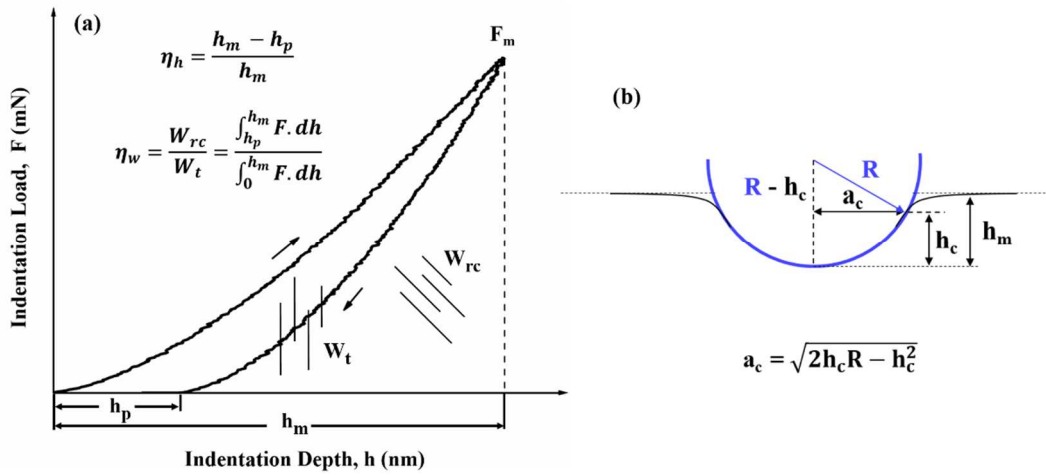
Fig. 4 EBSD inverse pole figures for recrystallized Ti2033 alloys at: (a) 973 K; (b) 1073 K; (c) 1173 K.

### 174 3.2 Grain size effect on superelasticity by nanoindentation

175 Combining EBSD orientation maps and nanoindentation tests, it is practically feasible  
176 to probe the superelasticity at the grain scale in localized region. The differently orientated  
177 grains show traceable grain boundaries under the microscope attached in nanoindentation  
178 platform, which facilitates the localization of the target grains with specific orientation  
179 identified from EBSD maps. Among the three specimens with different grain sizes, the areas  
180 with grains oriented or closely oriented in  $\langle 113 \rangle_{\beta}$  direction were selected and  
181 nanoindentation measurements were performed on those selected grains, so as to investigate  
182 the grain size effect on the superelastic behavior at grain scale.

183 To characterize the superelasticity of materials by nanoindentation, the depth recovery  
184 ratio  $\eta_h$  and the work recovery ratio  $\eta_w$  can be extracted from nanoindentation load-depth

185 ( $F-h$ ) curve [27], as highlighted in the schematic in Fig. 5a. Here,  $h_m$  denotes the maximum  
 186 indentation depth,  $h_p$  denotes the permanently residual depth. The total energy  $W_t$  and the  
 187 recoverable work  $W_{rc}$  are the integration area performed along the loading curve and the  
 188 unloading curve, respectively. The magnitude of  $W_{rc}$  indicates the capability of a superelastic  
 189 material to accommodate the deformation energy during indentation causing no damage  
 190 [28].



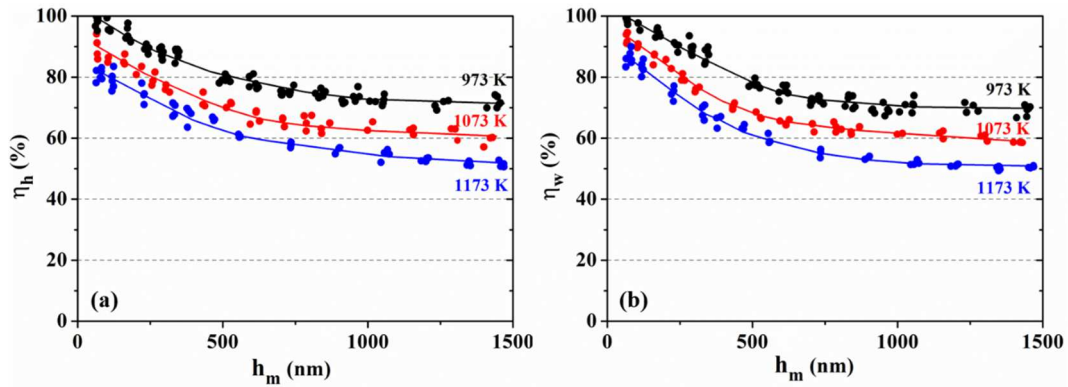
191

192 Fig. 5 (a) Schematic nanoindentation  $F-h$  curve and (b) schematic illustration of indentation upon loading  
 193 showing the parameters used for the analysis.

194 Nanoindentation matrices were performed with maximum indentation depth  $h_m$  varying  
 195 in the range of 50 - 1500 nm. The contact radius between the indenter and the specimen,  
 196  $a_c = \sqrt{2h_c R - h_c^2}$ , has been correspondingly calculated to be in range of 1.6 - 9.2  $\mu\text{m}$ . Here,  $h_c$   
 197 is the contact depth and  $R$  is the tip radius, as shown in Fig. 5b. Therefore, it is worth noting  
 198 that the real contact is mainly limited to the core of individual grains.

199 The  $\eta_h$  and  $\eta_w$  measurements were plotted as a function of  $h_m$  for the three Ti2033  
 200 specimens in Fig. 6. Each point represents the average value of at least 5 measurements.  
 201 Magnitudes of  $\eta_h$  and  $\eta_w$  deviate initially from the 100% line at very shallow depths, instead  
 202 of remaining at 100% value like the case of  $\eta_{\epsilon_{rec}}$  in Fig. 2b. It is probably due to the different  
 203 loading conditions applied during tensile testing and during nanoindentation. The tensile  
 204 testing corresponds to uniaxial stress condition while the nanoindentation produces rather  
 205 complex loading conditions with triaxial stress state and constant change of the deformed  
 206 volume. The stress of uniaxial tension testing is applied homogeneously in bulk and  
 207 increases gradually with applied strain  $\epsilon_{applied}$ , whereas during nanoindentation the spatial  
 208 stress field under indenter tip is distributed radially, decreasing along the radial direction.  
 209 Various studies [27, 29-31] modeled the deformation process underneath the indenter tip  
 210 using four concentric shells: a fully transformed and plastically deformed martensite region

211 right beneath the tip, surrounded by a fully transformed and reversible martensite region, a  
 212 partially transformed region and an untransformed parent  $\beta$  phase region. Therefore, once the  
 213 stress state beneath the indenter tip is beyond the critical stress for dislocation slips  $\sigma_{CSS}$ ,  
 214 plastic deformation occurs and, therefore, the recoverability decreases, even at very shallow  
 215  $h_m$ .



216

217 Fig. 6 Variations of depth recovery ratio  $\eta_h$  (a) and work recovery ratio  $\eta_w$  (b) versus maximum  
 218 indentation depth  $h_m$  for Ti2033 specimens recrystallized at 973 K, 1073 K and 1173 K, respectively.

219 Besides, it is also shown that the recovery ratios,  $\eta_h$  and  $\eta_w$ , for the three Ti2033 alloys  
 220 behave in the same way: decrease dramatically at low depths and saturate gradually at high  
 221 depths. The values of  $\eta_h$  and  $\eta_w$  vary from 100% to 70% for the Ti2033-973K alloy, from 95%  
 222 to 60% for the Ti2033-1073K alloy, and from 82% to 50% for the Ti2033-1173K alloy,  
 223 respectively. By comparison, the Ti2033 alloy subjected to different heat treatments  
 224 demonstrates the superelasticity characterized by nanoindentation in the following sequence:  
 225 Ti2033-973K > Ti2033-1073K > Ti2033-1173K, which is in agreement with the macroscale  
 226 recovery responses evaluated by tensile tests.

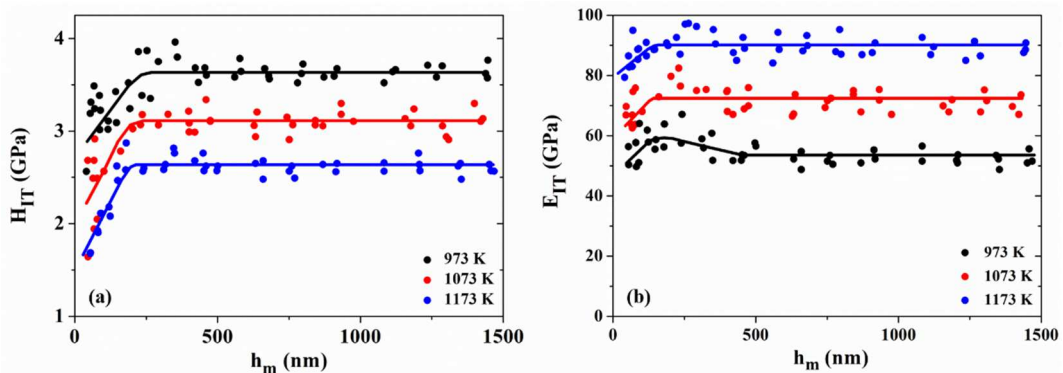
227 Nanoindentation is sensitive enough to probe the influence of grain size on the  
 228 recoverability. The grain size indeed affects the superelasticity in Ti2033 alloys. The  
 229 Ti2033-973K alloy with the smallest grain size exhibits the highest values of  $\eta_h$  and  $\eta_w$ ,  
 230 showing the highest superelasticity. Similar observation has been reported in  $\beta$   
 231 Ti-20Zr-12Nb-2Sn alloy [12]. It is due to that the critical stress for SIM transformation  $\sigma_{SIM}$   
 232 for the Ti2033-973K alloy has the lowest value and it increases with the increasing grain size  
 233 tailored by heat treatments, as discussed above. It has been sufficiently evidenced that the  
 234  $\sigma_{SIM}$  depends on various factors, such as alloying elements [32], test temperature [20],  
 235 presence of second phase [26, 33, 34], the strain rate [35], and grain size of  $\beta$  phase [16,  
 236 36-38]. In the present study, the focus is mainly on the analysis of the grain size effect on the  
 237  $\sigma_{SIM}$ . Several studies have made the supportive reports in agreement with our observations.  
 238 Bhattacharjee et al. [16] pointed out that the  $\sigma_{SIM}$  increases with increasing  $\beta$  grain size up to

239 300  $\mu\text{m}$  in Ti-10V-2Fe-3Al alloy. The dependence of  $\sigma_{SIM}$  on  $\beta$  grain size is related to the  
 240 free energy changes for the SIM transformation. Similarly, Gil et al. [37] observed a linear  
 241 increase in  $\sigma_{SIM}$  with increasing grain size. The elastic energy stored in grain boundary favors  
 242 SIM transformation. The transformed martensite interacts with grain boundaries, increases  
 243 the local elastic energy, and promotes the nucleation of new martensite. Wayman et al. [39]  
 244 also stated that grain boundaries could act as one of the most preferential nucleation sites in  
 245 martensitic transformation. Thus, grain refinement with higher density of grain boundaries  
 246 facilitates the SIM transformation.

247 In addition, the grain size influences the relative mobility of dislocations in the parent  
 248 and martensitic phases since the grain boundaries act as barriers for the dislocation  
 249 movements. Grain refinement increases the critical stress for dislocation slips  $\sigma_{CSS}$ , and thus  
 250 enhances the resistance to permanent plasticity deformation. Larger difference between the  
 251 critical stresses for plasticity deformation and for SIM transformation results in a larger  
 252 recovery strain in superelastic Ti-Nb-Ta alloy [40].

253 Therefore, it can be concluded that the higher critical stress for dislocation slips  $\sigma_{CSS}$  and  
 254 the lower critical stress for SIM transformation  $\sigma_{SIM}$  contribute to the excellent  
 255 superelasticity with a larger recovery strain in Ti2033-973K alloy with the smaller grain size.

256 The indentation hardness  $H_{IT}$  and modulus  $E_{IT}$  as a function of  $h_m$  have been extracted  
 257 according to Oliver-Pharr method [41], and plotted for the three Ti2033 alloys in different  
 258 grain sizes in Fig. 7. The smaller the grain size, the more grain boundaries underneath the  
 259 indenter tip. For instance, in the case of Ti2033-973K, the highest density of grain  
 260 boundaries will be involved during the indentation process. It is shown that Ti2033-973 K  
 261 with smallest grain size exhibits the highest  $H_{IT}$  and the lowest  $E_{IT}$ .



262  
 263 |Fig. 7 Indentation hardness  $H_{IT}$  (a) and modulus  $E_{IT}$  (b) versus maximum indentation depth  $h_m$  for Ti2033  
 264 specimens recrystallized at 973 K, 1073 K and 1173 K, respectively.

265 The variation of indentation hardness versus grain size is in agreement with Hall-Petch  
 266 relationship, which is also called grain refinement strengthening effect. This strengthening is  
 267 attributed to the blockage of dislocation motions by the high density of grain boundaries. For

268 superelastic materials involving the SIM transformation, indentation hardness reflects not  
269 only the resistance for the plastic deformation, but also the resistance for the phase  
270 transformation, and indentation modulus is the apparent modulus associated with the  
271 transformed volume fractions of  $\beta$  and  $\alpha''$  phases. The Ti2033-973 K alloy shows lowest  $E_{IT}$ ,  
272 probably due to its more prominent superelastic recovery accompanied by reversible SIM  
273 transformation that makes the material soft from the pseudo-elastic view.

## 274 **4 Conclusion**

275 In the present study, the superelastic Ti-20Zr-3Mo-3Sn (at. %) alloy was elaborated and  
276 subjected to different heat-treatments, and their microstructure presented the same strong  
277  $\{113\}_{\beta}<110>_{\beta}$  recrystallization texture but different average grain sizes were evidenced by  
278 EBSD. Investigation was performed to shed lights on the  $\beta$  grain size effect on the  
279 superelastic and mechanical properties. The main conclusions were made as follows:

280 (1) The evolution in the magnitude of the superelastic response probed by  
281 nanoindentation is in agreement with that measured by tensile tests. It confirms that  
282 nanoindentation can be used as an efficient tool to characterize the superelasticity and is  
283 sensitive enough to probe the grain size effect on the superelasticity.

284 (2) The superelastic behavior based on the reversible stress-induced martensitic  
285 transformation can be influenced by the grain size. The small-sized grains favor the  
286 martensitic transformation, resulting in high superelasticity.

287 (3) The alloy with smallest grain size exhibits the highest  $H_{IT}$  and the lowest  $E_{IT}$ .

288

## 289 **Acknowledgements**

290 Y. Zhou acknowledges the China Scholarship Council (CSC) for her Ph.D financial  
291 support (No. 201701810085). The authors also acknowledge the SCANMAT platform of the  
292 University of Rennes for providing access to SEM facilities.

293 **References**

- 294 [1] L. Héraud, P. Castany, D. Lailllé, T. Gloriant, In Situ Synchrotron X-ray Diffraction of  
295 the Martensitic Transformation in Superelastic Ti-27Nb and NiTi Alloys: A Comparative  
296 Study, *Materials Today: Proceedings*, 2 (2015) S917-S920.
- 297 [2] Y. Yang, P. Castany, M. Cornen, F. Prima, S.J. Li, Y.L. Hao, T. Gloriant, Characterization  
298 of the martensitic transformation in the superelastic Ti–24Nb–4Zr–8Sn alloy by in situ  
299 synchrotron X-ray diffraction and dynamic mechanical analysis, *Acta Materialia*, 88 (2015)  
300 25-33.
- 301 [3] S. Miyazaki, H.Y. Kim, H. Hosoda, Development and characterization of Ni-free Ti-base  
302 shape memory and superelastic alloys, *Materials Science and Engineering: A*, 438 (2006)  
303 18-24.
- 304 [4] Y. Al-Zain, H.Y. Kim, H. Hosoda, T.H. Nam, S. Miyazaki, Shape memory properties of  
305 Ti–Nb–Mo biomedical alloys, *Acta Materialia*, 58 (2010) 4212-4223.
- 306 [5] J. Fu, A. Yamamoto, H.Y. Kim, H. Hosoda, S. Miyazaki, Novel Ti-base superelastic  
307 alloys with large recovery strain and excellent biocompatibility, *Acta Biomaterialia*, 17  
308 (2015) 56-67.
- 309 [6] M.F. Ijaz, H.Y. Kim, H. Hosoda, S. Miyazaki, Effect of Sn addition on stress hysteresis  
310 and superelastic properties of a Ti–15Nb–3Mo alloy, *Scripta Materialia*, 72 (2014) 29-32.
- 311 [7] J.J. Gao, I. Thibon, D. Lailllé, P. Castany, T. Gloriant, Influence of texture and  
312 transformation strain on the superelastic performance of a new Ti–20Zr–3Mo–3Sn alloy,  
313 *Materials Science and Engineering: A*, 762 (2019) 138075.
- 314 [8] M.F. Ijaz, H.Y. Kim, H. Hosoda, S. Miyazaki, Superelastic properties of biomedical (Ti–  
315 Zr)–Mo–Sn alloys, *Materials Science and Engineering: C*, 48 (2015) 11-20.
- 316 [9] H. Kim, Y. Ikehara, J.I. Kim, H. Hosoda, S. Miyazaki, Martensitic transformation, shape  
317 memory effect and superelasticity of Ti–Nb binary alloys, *Acta Materialia*, 54 (2006)  
318 2419-2429.
- 319 [10] H.Y. Kim, T. Sasaki, K. Okutsu, J.I. Kim, T. Inamura, H. Hosoda, S. Miyazaki, Texture  
320 and shape memory behavior of Ti–22Nb–6Ta alloy, *Acta Materialia*, 54 (2006) 423-433.
- 321 [11] T. Waitz, T. Antretter, F.D. Fischer, N.K. Simha, H.P. Karnthaler, Size effects on the

322 martensitic phase transformation of NiTi nanograins, *Journal of the Mechanics and Physics*  
323 *of Solids*, 55 (2007) 419-444.

324 [12] J.J. Gao, I. Thibon, P. Castany, T. Gloriant, Effect of grain size on the recovery strain in  
325 a new Ti - 20Zr-12Nb-2Sn superelastic alloy, *Materials Science and Engineering: A*, 793  
326 (2020) 139878.

327 [13] F. Sun, S. Nowak, T. Gloriant, P. Laheurte, A. Eberhardt, F. Prima, Influence of a short  
328 thermal treatment on the superelastic properties of a titanium-based alloy, *Scripta Materialia*,  
329 63 (2010) 1053-1056.

330 [14] Q. Sun, A. Aslan, M. Li, M. Chen, Effects of grain size on phase transition behavior of  
331 nanocrystalline shape memory alloys, *Science China Technological Sciences*, 57 (2014)  
332 671-679.

333 [15] T. Grosdidier, Y. Combres, E. Gautier, M.J. Philippe, Effect of microstructure variations  
334 on the formation of deformation-induced martensite and associated tensile properties in a  $\beta$   
335 metastable Ti alloy, *Metallurgical and Materials Transactions A*, 31 (2000) 1095-1106.

336 [16] A. Bhattacharjee, S. Bhargava, V.K. Varma, S.V. Kamat, A.K. Gogia, Effect of  $\beta$  grain  
337 size on stress induced martensitic transformation in  $\beta$  solution treated Ti-10V-2Fe-3Al alloy,  
338 *Scripta Materialia*, 53 (2005) 195-200.

339 [17] X. Bian, A.A. Gazder, A.A. Saleh, E.V. Pereloma, A comparative study of a NiTi alloy  
340 subjected to uniaxial monotonic and cyclic loading-unloading in tension using digital image  
341 correlation: The grain size effect, *Journal of Alloys and Compounds*, 777 (2019) 723-735.

342 [18] P.J.S. Buenconsejo, R. Zarnetta, A. Ludwig, The effects of grain size on the phase  
343 transformation properties of annealed (Ti/Ni/W) shape memory alloy multilayers, *Scripta*  
344 *Materialia*, 64 (2011) 1047-1050.

345 [19] Y. Zhou, A. Fillon, D. Laillé, T. Gloriant, Crystallographic anisotropy of the superelastic  
346 and mechanical properties of the Ti-20Zr-3Mo-3Sn alloy evidenced by nanoindentation at  
347 the grain scale, *Journal of Alloys and Compounds*, 892 (2022) 162112.

348 [20] T.W. Duerig, J. Albrecht, D. Richter, P. Fischer, Formation and reversion of stress  
349 induced martensite in Ti-10V-2Fe-3Al, *Acta Metallurgica*, 30 (1982) 2161-2172.

350 [21] T. Grosdidier, C. Roubaud, M.-J. Philippe, Y. Combres, The deformation mechanisms in  
351 the  $\beta$ -metastable  $\beta$ -Cez titanium alloy, *Scripta Materialia*, 36 (1997) 21-28.

352 [22] J.-L. Liu, H.-Y. Huang, J.-X. Xie, The roles of grain orientation and grain boundary  
353 characteristics in the enhanced superelasticity of Cu<sub>71.8</sub>Al<sub>17.8</sub>Mn<sub>10.4</sub> shape memory alloys,  
354 *Materials & Design*, 64 (2014) 427-433.

355 [23] L.L. Pavón, E.L. Cuellar, S.V. Hernandez, I.E. Moreno-Cortez, H.Y. Kim, S. Miyazaki,  
356 Effect of heat treatment condition on microstructure and superelastic properties of  
357 Ti<sub>24</sub>Zr<sub>10</sub>Nb<sub>2</sub>Sn, *Journal of Alloys and Compounds*, 782 (2019) 893-898.

358 [24] H.Y. Kim, J.I. Kim, T. Inamura, H. Hosoda, S. Miyazaki, Effect of thermo-mechanical  
359 treatment on mechanical properties and shape memory behavior of Ti-(26–28)at.% Nb  
360 alloys, *Materials Science and Engineering: A*, 438-440 (2006) 839-843.

361 [25] H. Jabir, A. Fillon, P. Castany, T. Gloriant, Crystallographic orientation dependence of  
362 mechanical properties in the superelastic Ti-24Nb-4Zr-8Sn alloy, *Physical Review Materials*,  
363 3 (2019) 063608.

364 [26] C. Li, X. Wu, J.H. Chen, S. van der Zwaag, Influence of  $\alpha$  morphology and volume  
365 fraction on the stress-induced martensitic transformation in Ti-10V-2Fe-3Al, *Materials*  
366 *Science and Engineering: A*, 528 (2011) 5854-5860.

367 [27] Y. Zhou, A. Fillon, H. Jabir, D. Laillé, T. Gloriant, Investigation of the superelastic  
368 behavior of a Ti-16Zr-13Nb-2Sn sputtered film by nanoindentation, *Surface and Coatings*  
369 *Technology*, (2020) 126690.

370 [28] R. Liu, D.Y. Li, Y.S. Xie, R. Llewellyn, H.M. Hawthorne, Indentation behavior of  
371 pseudoelastic TiNi alloy, *Scripta Materialia*, 41 (1999) 691-696.

372 [29] C. Maletta, F. Furgiuele, E. Sgambitterra, M. Callisti, B. Mellor, R. Wood, Indentation  
373 response of a NiTi shape memory alloy: modeling and experiments, *Frattura ed Integrità*  
374 *Strutturale*, 6 (2012) 5-12.

375 [30] Q. Kan, W. Yan, G. Kang, Q. Sun, Oliver–Pharr indentation method in determining  
376 elastic moduli of shape memory alloys—A phase transformable material, *Journal of the*  
377 *Mechanics and Physics of Solids*, 61 (2013) 2015-2033.

378 [31] G.A. Shaw, D.S. Stone, A.D. Johnson, A.B. Ellis, W.C. Crone, Shape memory effect in  
379 nanoindentation of nickel–titanium thin films, *Applied Physics Letters*, 83 (2003) 257-259.

380 [32] A. Paradkar, S.V. Kamat, A.K. Gogia, B.P. Kashyap, Effect of Al and Nb on the trigger  
381 stress for stress-induced martensitic transformation during tensile loading in Ti–Al–Nb



382 alloys, *Materials Science and Engineering: A*, 487 (2008) 14-19.

383 [33] A. Paradkar, S. Kamat, A. Gogia, B. Kashyap, Effect of Volume Fraction of Primary  $\alpha_2$   
384 on the Trigger Stress for Stress-Induced Martensitic Transformation in Two-Phase Ti-Al-Nb  
385 Alloys, *Metallurgical and Materials Transactions A*, 39 (2008) 2086-2094.

386 [34] Y. Yang, P. Castany, E. Bertrand, M. Cornen, J.X. Lin, T. Gloriant, Stress  
387 release-induced interfacial twin boundary  $\omega$  phase formation in a  $\beta$  type Ti-based single  
388 crystal displaying stress-induced  $\alpha''$  martensitic transformation, *Acta Materialia*, 149 (2018)  
389 97-107.

390 [35] A. Paradkar, S.V. Kamat, The effect of strain rate on trigger stress for stress-induced  
391 martensitic transformation and yield strength in Ti-18Al-8Nb alloy, *Journal of Alloys and*  
392 *Compounds*, 496 (2010) 178-182.

393 [36] A. Paradkar, S. Kamat, A. Gogia, B. Kashyap, Trigger stress for stress-induced  
394 martensitic transformation during tensile deformation in Ti-Al-Nb alloys: Effect of grain size,  
395 *Metallurgical and Materials Transactions A*, 39 (2008) 551-558.

396 [37] F.J. Gil, J.A. Planell, Behaviour of normal grain growth kinetics in single phase titanium  
397 and titanium alloys, *Materials Science and Engineering: A*, 283 (2000) 17-24.

398 [38] M.-H. Cai, C.-Y. Lee, Y.-K. Lee, Effect of grain size on tensile properties of  
399 fine-grained metastable  $\beta$  titanium alloys fabricated by stress-induced martensite and its  
400 reverse transformations, *Scripta Materialia*, 66 (2012) 606-609.

401 [39] C. Wayman, H. Bhadeshia, Phase transformations, nondiffusive, in: *Physical*  
402 *Metallurgy*, Elsevier, 1996, pp. 1507-1554.

403 [40] H.Y. Kim, S. Hashimoto, J.I. Kim, T. Inamura, H. Hosoda, S. Miyazaki, Effect of Ta  
404 addition on shape memory behavior of Ti-22Nb alloy, *Materials Science and Engineering: A*,  
405 417 (2006) 120-128.

406 [41] W.C. Oliver, G.M. Pharr, Measurement of hardness and elastic modulus by  
407 instrumented indentation: Advances in understanding and refinements to methodology,  
408 *Journal of Materials Research*, 19 (2004) 3-20.

409

410